Corrosion Inhibition at Scribed Locations in Coated AA2024-T3 by Cerium- and DMTD-Loaded Natural Silica Microparticles under Continuous Immersion and Wet/Dry Cyclic Exposure

Denissen, Paul J.; Shkirskiy, Viacheslav; Volovitch, Polina; Garcia, Santiago J.

DOI
10.1021/acsami.0c03368

Publication date
2020

Document Version
Final published version

Published in
ACS applied materials & interfaces

ACS APPLIED MATERIALS & INTERFACES

www.acsami.org

Research Article

Corrosion Inhibition at Scribed Locations in Coated AA2024-T3 by Cerium- and DMTD-Loaded Natural Silica Microparticles under Continuous Immersion and Wet/Dry Cyclic Exposure

Paul J. Denissen,* Viacheslav Shkirskiy, Polina Volovitch, and Santiago J. Garcia*

Cite This: *ACS Appl. Mater. Interfaces* 2020, 12, 23417−23431

Read Online

ACCESS | Metrics & More | Article Recommendations | Supporting Information

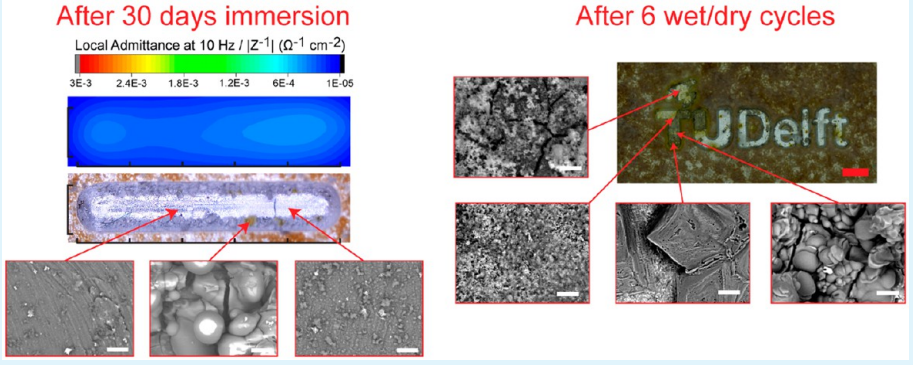

ABSTRACT: Earlier studies on cerium-loaded naturally occurring silica microparticles (i.e., diatomaceous earth) demonstrated the potential to efficiently protect small scratches in epoxy-coated AA2024-T3 panels during relatively short immersion times. The current work investigates the potential of such inhibitor-loaded microparticles to protect wide and deep scribes (up to 1 mm wide) in long-time immersion testing and during cyclic (wet/dry) conditions. For this, cerium nitrate and 2,5-dimercaptothiadiazole (DMTD) were used as inorganic and organic corrosion inhibitors. The corrosion protection was evaluated using a hyphenated real-time optics/electrochemistry method and two individual local techniques measuring oxygen concentration and electrochemical impedance (LEIM) inside the scribe. SEM/EDS was used to analyze the samples after exposure. The results show significant levels of corrosion protection at damaged locations at low cerium concentrations (3.7 wt % Ce^{3+} relative to the total coating mass) during 30 days of immersion in salt solution. However, for a given scribe geometry, the protection was found to be dependent on the electrolyte volume with larger electrolyte/exposed metal ratios leading to short protection time. A partial replacement of the Ce^{3+} by DMTD in the microcarriers resulted in a higher degree of passivation than when DMTD was used alone. Wet/dry cyclic exposure tests showed that cyclic conditions can increase the buildup of stable inhibitor-containing layers in the case of cerium-loaded silica microparticles. This underlines the need for more research using wet/dry exposure conditions.

KEYWORDS: *DMTD, cerium, self-healing, inhibitor, local electrochemistry*

1. INTRODUCTION

The wish and legal need to find less harmful but still efficient alternatives to carcinogenic hexavalent chromium salts as corrosion inhibitors in anticorrosive primers on aluminum aircraft alloys and other metals has triggered many studies in recent years.[1,2] Potentially acceptable alternatives such as lanthanide salts (e.g., Ce, Y, La, Pr, and Nd),[3−5] Li salts,[6−10] and organic compounds[11−16] have been identified and studied during the last decades. Nevertheless, these alternatives are generally less effective, work under limited environmental conditions (e.g., pH), and lose part of their efficiency when incorporated in polymeric matrixes (coatings) due to unwanted physical/chemical inhibitor−coating interactions and uncontrolled release.[16,17] These challenges have been addressed by the development of numerous nanosized encapsulation methods that reduce the unwanted inhibitor−coating interactions and allow for controlled release, from discrete use of nanoparticles to electrospun nanofiber mats.[8,12,18−21]

In our previous work, we showed that naturally occurring nanoporous, hollow, silica microparticles (diatomaceous earth or DE) can also act as a container for corrosion inhibitors such

Received: February 21, 2020
Accepted: April 23, 2020
Published: April 23, 2020

Table 1. Coatings Formulation Given as a Function of Epikote 828 Resin[a]

sample name	inhibitor salt	Ancamine 2500 (phr)	DE particles (phr)	DE container (phr)	inhibitor (phr)	inhibiting active component (wt %)	thickness (μm)
epoxy		58					73 ± 5
DE		58	48	48	0		65 ± 5
DMTD-DE	DMTD	58	48	24	24	11.5	77 ± 5
0.5Ce-DE\ 0.5DMTD-DE	$Ce(NO_3)_3$ and DMTD	58	48	24	12 Ce + 12 DMTD	2.1 + 5.8	50 ± 5
Ce-DE	$Ce(NO_3)_3$	58	48	24	24	3.7	69 ± 5
0.50Ce-DE	$Ce(NO_3)_3$	58	24	12	12	2.1	79 ± 5
0.16Ce-DE	$Ce(NO_3)_3$	58	8	4	4	0.8	72 ± 5

[a]phr = parts per hundred epoxy resin in weight. This table includes the calculated inhibitor content in phr and the calculated content of inhibiting active component (DMTD or Ce^{3+}) in wt % of the total coating weight.

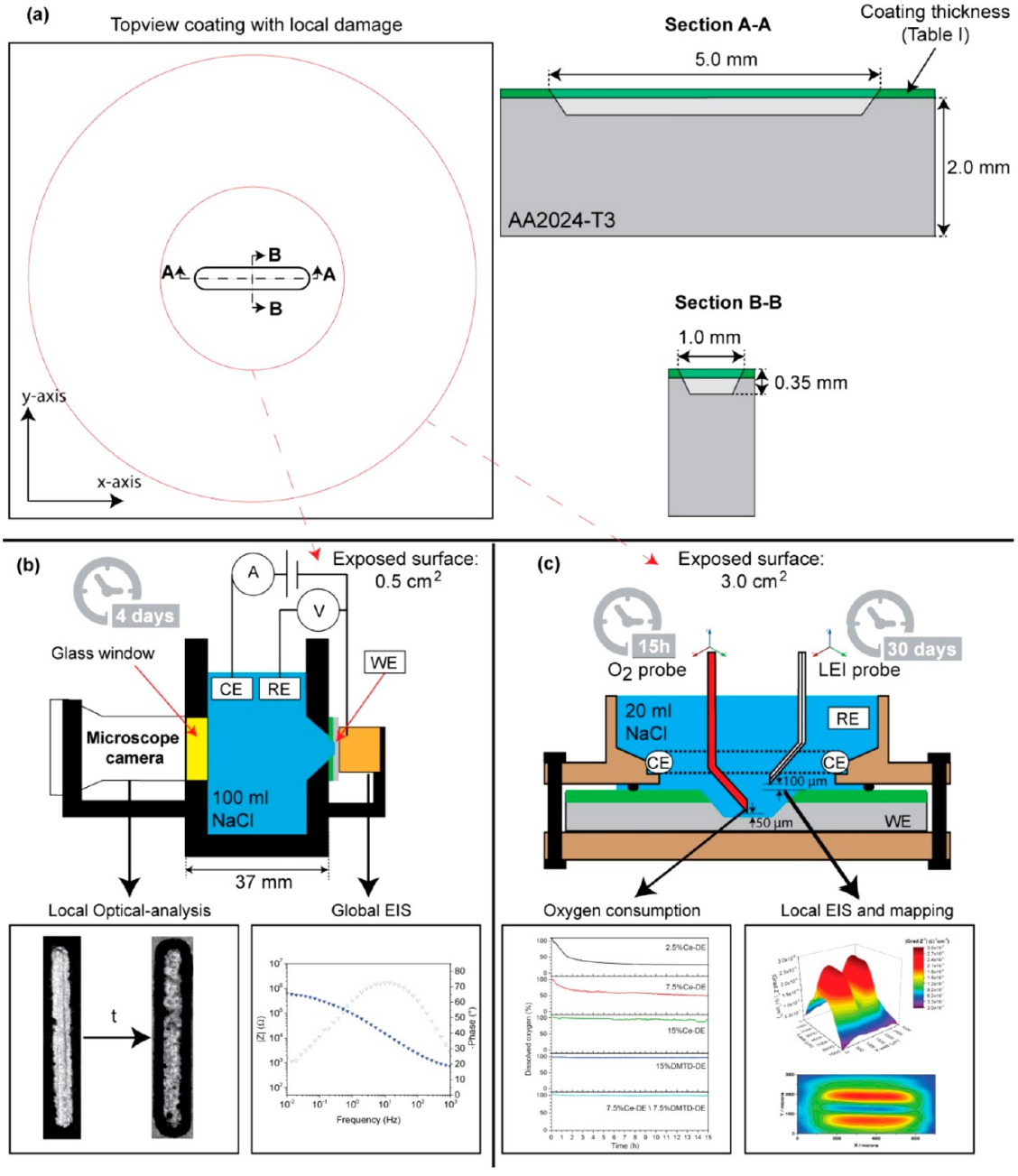

Figure 1. (a) Schematics of local scribe dimensions and exposed areas used in the different cells shown in (b) and (c); (b) optical-electrochemical cell with raw information obtained in the form of pictures and Bode plot; and (c) horizontal cell used for the local oxygen concentration and LEIS/LEIM tests.

https://dx.doi.org/10.1021/acsami.0c03368
ACS Appl. Mater. Interfaces 2020, 12, 23417−23431

as cerium nitrate ($Ce(NO_3)_3$), an efficient corrosion inhibitor for Cu-rich aluminum alloys such as AA2024-T3.[22] When such loaded DE particles are mixed with an epoxy-amine, a coating with high corrosion inhibiting power was obtained. The degree of unwanted side reactions between the cerium-inhibitor in the containers and the matrix was lower than those observed for cerium salts directly added to epoxy/amine coatings. This allowed sufficient quantities of Ce^{3+} ions to diffuse to the metallic substrate at scribe locations to protect the metal in the presence of corrosive electrolytes (0.05 M NaCl). This first study on DE particles as an effective container for non-carcinogenic corrosion inhibitors served as a proof of principle. Nevertheless, the corrosion protection was just monitored for one inhibitor−carrier combination, small scratches (130 μm wide scratches) and under continuous exposure to relatively large electrolyte volumes for short immersion times (up to 4 days).

The present work aims to expand this initial study and to investigate the effect of some other important parameters influencing the corrosion protection. Here, we focus on the effect of (i) large-scale scribes (i.e., 1 mm wide and 300 μm below the coating layer), (ii) the use of inorganic and organic inhibitors, $Ce(NO_3)_3$ (Ce) and 2,5-dimercaptothiadiazole (DMTD) loaded inside DE particles, (iii) the amount of the electrolyte volume to which a scribe is exposed during continuous (wet-) exposure up to 30 days of immersion, and (iv) the corrosion protection in case of multiple wet/dry cycles. The latter, not very common in scientific reports, was prompted by past literature[23−26] that showed that corrosion protection during continuous wet exposure can be quite different from that under cyclic wet/dry conditions. We monitored the evolution of the damaged coatings immersed in electrolyte and quantified the corrosion extent and kinetics, using a previously reported hyphenated real-time optics/electrochemistry method.[22,27,28] To gain more information on the local corrosion processes, we locally measured the time evolution of the oxygen concentration at the bottom of the scribe inspired by previous works[29] and performed electrochemical impedance mapping (LEIM) at the scribes.[30,31] SEM/EDS was used to analyze the samples after exposure and to obtain more information on the inhibitor−substrate interactions.

2. EXPERIMENTAL SECTION

2.1. Materials. Diatomaceous earth (DE) of the type Diafil 525, mainly belonging to the *Aulacoseiraceae* family, was supplied by Profiltra Customized Solutions (NL). The DE was refined following the procedure reported elsewhere.[22] The resulting refined DE consisted primarily of intact hollow cylindrical micro- and nanoporous amorphous silica structures with a mean particle size of 12 μm with nanopores around 500 nm in diameter, evenly distributed around the wall structure.[32] Cerium nitrate hexahydrate ($Ce(NO_3)_3{\cdot}6H_2O$) and 2,5-dimercapto-1,3,4-thiadiazole (DMTD) were used as corrosion inhibitors. Three millimeter thick industrial grade aluminum alloy 2024-T3 sheets were supplied by Kaizer Aluminum. The plates were cut into 200 × 250 mm panels, grinded using 320 grit SiC paper, degreased with acetone, sonicated for 30 min at 60 °C in ethanol, and air-dried. After being dried, the panels were exposed to NaOH for 10 s, rinsed with demi-water, and dried under nitrogen for pseudoboehmite treatment prior to the coating application. Commercially available bisphenol A-based epoxy resin (Epikote 828) and amine cross-linker (Ancamine2500) were supplied by AkzoNobel (NL) and used as-received to form the coating binder using xylene (99%) as solvent. Milipore filtered water (electrical resistivity 18 MΩ cm) was employed in all steps requiring water.

2.2. Inhibitor Loading and Coatings Preparation. *DE Loading with Inhibitors.* Three batches of DE particles were prepared: unloaded DE particles and inhibitor-loaded DE containing either $Ce(NO_3)_3{\cdot}6H_2O$ or DMTD. A mixture of 5 g of DE and 5 g of inhibitor was added to 10 mL of dimethylformamide (DMF, ≥99.9%) and stirred for 24 h at 320 rpm using a shaking table. Next, the mixture was spread on a glass plate with a glass pipet and distributed with a 100 μm spiral bar coater. Drying at 60 °C for 30 min led to a thin layer of dry DE particles loaded with corrosion inhibitors. The DE layer was removed from the plate with a spatula, and the resulting powder was further dried for another 72 h at 60 °C and stored in a desiccator prior to use. As a result, DE particles with 50 wt % inhibitor salt were obtained.

Coatings and Controlled Damages to the Coated Panels. Table 1 shows the different coating compositions used in this study. Besides the phr content of loaded DE particles, the table shows the derived (calculated) content of DE microcarrier and inhibitor in phr and the thereby resultant content of inhibiting active species in the coating in wt %. The latter was calculated on the basis of the available inhibitor (in weight) in the container inside the coating but considering only the main inhibiting component of the salt (i.e., Ce^{3+} available in cerium salt). Details of the calculations can be found in the Supporting Information (eq S1).

A Roland EGX-350 engraver equipped with a conical cemented carbide tip of 0.25 mm in radius (ZECA-2025BAL) rotating at 15 000 rpm was used to create controlled scribes on the coated panels. Scribes of 1.0 mm wide, 5.0 mm long, and 0.35 mm deep (i.e., well into the metallic substrate) with respect to the coated surface were created without causing lateral delamination (Figure 1a). The resulting chips from the engraved zone were removed from the surface by air blowing. For the wet−dry cyclic test, the TU Delft logo was engraved using the same setup but with a smaller tip (0.13 mm in radius, ZECA-2013BAL) and a depth of 0.15 mm with respect to the coating surface (i.e., still well below the metal surface).

General Characterization of the Loaded DE Particles and Coatings. The inhibitor-loaded microparticles were evaluated using a JEOL SJM-840 scanning electron microscope (SEM) coupled with energy dispersive X-ray spectroscopy (SEM-EDS) at 5 kV and a Renishaw inVia confocal Raman spectrometer equipped with a 32 mW laser source at 532 nm and a Leica objective of 50× magnification and numerical aperture of 0.55. In the case of the Raman analysis, an effective laser power of 10% was employed for 1 s excitation over 3 accumulations per point (i.e., three times of 1 s exposure).

Cross sections of the as-prepared coatings were analyzed by SEM-EDS at 5 kV after they were dry-grinded up to grit 4000 with SiC paper. The coatings were analyzed for a second time after being manually wet-polished for 20 s to a final roughness of 1 μm. A surface analysis of the scribes after exposure (immersion and wet/dry cycles) was performed using a JEOL JSM-IT100 SEM-EDS in backscattered electron mode (BSE) at 20 kV.

2.3. Corrosion Tests. *Exposure to Large Electrolyte Volumes (200 mL/cm^2) and Short Immersion Times.* A recently developed 3D printed electrochemical cell combining electrochemical characterization and real-time optics (Figure 1b) was used to monitor the corrosion behavior at the scribes during continuous immersion (up to 4 days). The details of the hardware used for the testing and the protocol used to extract quantitative information from the under-immersion continuous imaging can be found elsewhere.[27,28] The exposed area to the electrolyte, including the scribe, was 0.5 cm^2, whereby 100 mL of 0.05 M NaCl aqueous solution was used (i.e., 200 mL/cm^2). The samples were placed vertically with the long side of the scribes perpendicular to the base (Figure 1) to avoid the deposition of oxide and inhibitor products inside the scribe due to gravity. All experiments were conducted at room temperature (20 ± 2 °C) under ambient conditions.

A potentiostat Metrohm PGSTAT 302 and a Dino-Lite AM7915MZT USB-camera with a 5.0 megapixel CMOS sensor (2592 × 1944 pixels) were used for electrochemical tests and optical monitoring of the corrosion reactions. The camera and the

https://dx.doi.org/10.1021/acsami.0c03368
ACS Appl. Mater. Interfaces 2020, 12, 23417−23431

electrochemical cell were both placed inside a Faraday cage to avoid external electrical interferences. A three-electrode setup was used consisting of a saturated Ag/AgCl reference electrode (RE), 6.6 mm diameter porous graphite rod as counter electrode (CE), and the scribed coated sample as working electrode (WE). This equipment allowed one to perform electrochemical impedance spectroscopy (EIS) and open circuit potential (OCP) measurements (i.e., global electrochemistry)[27] in parallel to the optical monitoring. EIS and OCP measurements, each taken at 10−15 min, were performed every 60 min in case of stable OCP values (dE/dt < 0.1 mV/s). EIS was performed in the frequency range 10^5−10^{-2} Hz at an amplitude of 10 mV root-mean-square (RMS) over OCP to minimize the influence of the test on the metal-coating system while still obtaining a reliable response. The potentiostat was controlled via a USB interface through the software package NOVA V1.11.1. A high-resolution optical camera placed in front of the scribe and the DinoCapture 2.0 software package allowed one to capture images (1 pixel = 3 μm) of the scribe surface every 5 min while simultaneously performing the electrochemical tests.

The photographs of the scribes were further analyzed using a previously reported optical analysis protocol.[27,28,33] This allowed one to obtain highly space-temporally resolved quantitative information of the corrosion and inhibition processes in the form of "area changed as a function of time". This information is here presented in the form of color maps of the scribes. To quantify the extent and kinetics of the optically detectable surface phenomena (e.g., pits, corrosion products, and/or inhibitor deposition), the so-called "changed surface area" ($S_{changed}$) parameter was calculated over time using eq 1:

$$S_{changed}|_t\ (\%) = \frac{N_t}{N} * 100\% \quad (1)$$

where N_t is the number of changed pixels at time t and N is the total amount of analyzed pixels.

Exposure to Small Electrolyte Volumes (6.67 mL/cm^2) and Long Immersion Times. Local electrochemistry (LEIS/LEIM) and oxygen concentration measurements at the scribe were performed using a horizontally positioned 3D printed cell (Figure 1c). It is important to note that the horizontal position was necessary for the local measurements. The effect of the horizontal versus vertical position on the overall inhibition should be studied in more detail in future works. Because of the configuration of the cell and the nature of local electrochemistry testing, the setup implied the exposure of a larger area than in the optical-electrochemical setup (3 cm^2) but to a lower electrolyte volume (20 mL, 0.05 M NaCl) with a film thickness of 3 cm. This resulted in 6.67 mL/cm^2, near 30 times less than that in the optical-electrochemical setup.

Local concentrations of dissolved oxygen in solution were measured using an optical oxygen detector from PyroScience (OXB50) equipped with a 50−70 μm bare fiber microsensor (OXB50) and external 4-wire PT100 temperature sensor. To offer some mechanical support and protection against accidental contact during mounting, the optical fiber was embedded in a glass microcapillary. The probe was positioned with a motorized stage from Sensolitics and located at the center of the scribe, 50 μm above the metal surface. The temperature sensor was placed inside the electrolyte and used to calculate the oxygen signal under fluctuating temperatures between 21 ± 4 °C using the built-in software. The oxygen levels were recorded every 3 s, while the sample and probe were kept stationary to avoid the migration of electrolyte over a period of 15 h.

Local electrochemical impedance measurements were performed on a new batch of scribed coatings. A detailed description of the setup can be found elsewhere.[31] An in-house-developed probe was placed and controlled in the x, y, z directions with the help of a Sensolitics system reaching a precision of 1 μm in each axis. The probe was positioned 100 ± 1 μm above the coating surface. This was achieved by lowering the probe with 1 μm steps until it reached the coating surface, followed by a 100 μm upward displacement. Control measurements at heights of 110 and 90 μm showed that the obtained admittance values varied less than 1%, thereby showing the robustness of the method with height variations. The probe consists of two vertically displaced 200 μm diameter Ag/AgCl wires allowing for higher spatial resolution as compared to commercially available probes.[34] When scanning the sample surface, the probe moved with a rate of 0.075 mm/s in the x-direction and a step-size of 0.100 mm in the y-direction. The z-position was not changed during scanning. The measurements were performed using a standard three-electrode setup combined with the probe connected to the auxiliary channels of a Solatron potentiostat XM 1MS/s with FRA, under the control of interfaced built-in OWISoft and XM-studio software. The three-electrode configuration consisted of a saturated Ag/AgCl reference electrode, platinum wire with a surface area of 50 mm^2 as counter electrode, and the scribed coated sample as working electrode. The measurements were performed using two different protocols: (i) local electrochemical impedance spectroscopy (LEIS) with the probe in a stationary position at the center of the scribe while performing a traditional EIS measurement at a frequency range of 10^5−10^{-2} Hz, whereby the points around 60 Hz were not taken into account because harmonics from external electrical equipment interfered with the measurements, and (ii) local electrochemical impedance mapping (LEIM) by moving the probe across a designated area of the scribed coating at a resolution of 0.075 × 0.100 mm per measured point while performing an impedance measurement at a fixed excitation of 10 Hz. An amplitude similar to the global impedance (10 mV RMS) was found insufficient to obtain stable admittance values from the local probe at low frequencies. It was thereby decided to increase the admittance to 30 mV peak-to-peak while still obtaining a reliable and identical EIS response using the RE as compared to 10 mV RMS.

The local potential difference between the wires of the probe (ΔV_{probe}) was scaled to local current densities (i_{loc}) through Ohm's law and used to calculate the local impedance per imposed frequency (ω). This involves the potential measured with respect to the reference electrode as shown in eq 2 and described in more detail elsewhere.[16]

$$Z(\omega) = \frac{\tilde{V}(\omega) - \Phi_{ref}}{i_{loc}(\omega)} = \frac{\tilde{V}(\omega)}{\Delta V_{probe}(\omega)} * \frac{d}{k} \quad (2)$$

where $\tilde{V}(\omega) - \Phi_{ref}$ represents the potential difference between the WE and the RE in the bulk solution, d is the distance between the two probes, and k is the electrolyte conductivity of the electrolyte.

The calculations to reconstruct the local impedance spectra and maps were performed with a dedicated Python script using the time-stamps from impedance measurements and the defined position of the probe from the positioning module.[31] The gradient and magnitude of the local admittance (inverse of impedance) were mapped as a function of the x- and y-positions. Admittance magnitudes were used rather than impedance so that the area of increased electrochemical activity generally appeared as peaks.[31]

Wet/Dry Cyclic Tests. Wet/dry cyclic corrosion tests were performed on the best performing coating according to the long-term immersion testing. This allowed one to study the stability of the inhibiting layer at the scribed site under discontinuous immersion conditions. For this, the electrochemical cell with small electrolyte volumes (6.67 mL/cm^2) was used. Each cycle (6 in total) consisted of (i) exposure to 0.05 M NaCl electrolyte, (ii) electrolyte removal, coating washing with demineralized water, and blowing with air, and (iii) drying under ambient conditions for 5 h. The exposure time of each immersion step (wet) is shown in Table 2 and resulted in a total immersion period of 13 days. After each wet exposure, photos of the scribes were taken with a digital microscope Keyence VHX-2000E using a VH-Z20R lens. At the end of the cyclic test, the scribes were analyzed by SEM/EDS.

3. RESULTS AND DISCUSSION

3.1. DE Loading, Release, and Coating Evaluation.

Figure 2 shows representative SEM images, EDS spectra, and Raman results for the hollow diatomaceous earth (DE) microparticles before and after inhibitor loading with cerium

https://dx.doi.org/10.1021/acsami.0c03368
ACS Appl. Mater. Interfaces 2020, 12, 23417−23431

Table 2. Exposure Time of Each Wet Step during the Wet/Dry Cyclic Exposure

cycle	immersion step duration in days
1	2
2	1
3	2
4	3
5	1
6	4

salt and DMTD. A clearly visible layer with a high content of cerium is observed on the surface and pores of the Ce-loaded DE particles (Figure 2b and d). No inhibitor film around the particles surface was detected with SEM/EDS for the case of DMTD-modified DE (Figure 2c). Raman analysis (Figure 2e), however, confirmed the presence of the DMTD by the detection of high intensity peaks corresponding to the vibrational signals of DMTD as reported elsewhere.[35] This suggests a higher loading inside the particles than in the case of the cerium-loaded DE. Volumetric calculations on inhibitor-loaded microparticles indicate that less than 2 vol % of the available internal volume is filled with inhibitor. This highlights that higher loadings per particle can be expected when using improved loading protocols.

Figure 3 shows SEM/EDS micrographs of the epoxy coatings containing DE, Ce-DE, DMTD-DE, and 0.5Ce-DE \0.5DMTD-DE after dry (Figure 3a) and wet polishing (Figure 3b). The DE particles appear as silica clusters with a diameter between 5 and 30 μm distributed homogeneously over the entire cross section of the coating in the case of the nonloaded DE, and as highly agglomerated particles in the case of the Ce-DE. Higher levels of silica are detectable by EDS in the case of nonloaded DE than for the inhibitor-loaded ones. This is in good agreement with the higher DE microparticle loading in the case of the nonloaded DE coating (see Table 1, 48 phr DE microparticles vs 24 phr). Moreover, when wet polishing was used (Figure 3b), large open spaces appeared in and around the inhibitor-loaded DE particles. We attribute this effect to the local dissolution of cerium and DMTD salts and the removal of the surrounding coating matrix by the small amount of ethanol used during polishing. These results confirm that the inhibitors are located inside and around the DE particles after dispersion in the epoxy/amine coating.

3.2. Global Electrochemistry and Spatially Resolved Real-Time Optics: Exposure to Large Electrolyte Volume per Exposed Damaged Area. Figure 4 shows selected EIS Bode plots (|Z| and phase) of the studied coatings after 3 h (Figure 4a) and 90 h (Figure 4b) of immersion obtained with the optical-electrochemical setup (Figure 1b). The corresponding Nyquist plots can be found in Figure S1. The coating with unloaded DE is not shown because the results are comparable to those of the unloaded epoxy reference coating.

At short immersion times (3 h, Figure 4a), the sample containing two inhibitors (0.5Ce-DE\0.5DMTD-DE) shows the highest total impedance. This is closely followed by the coating containing cerium at the same total inhibitor phr content but near 2 times more cerium in wt %, Ce-DE, and the sample containing one-half the total inhibitor phr content (0.5Ce-DE). Interestingly, the phase angle for 0.5Ce-DE \0.5DMTD-DE is less broad and more located toward lower frequencies than the phase of Ce-DE and 0.5Ce-DE, which also shows an equally broad phase angle. The sample with the

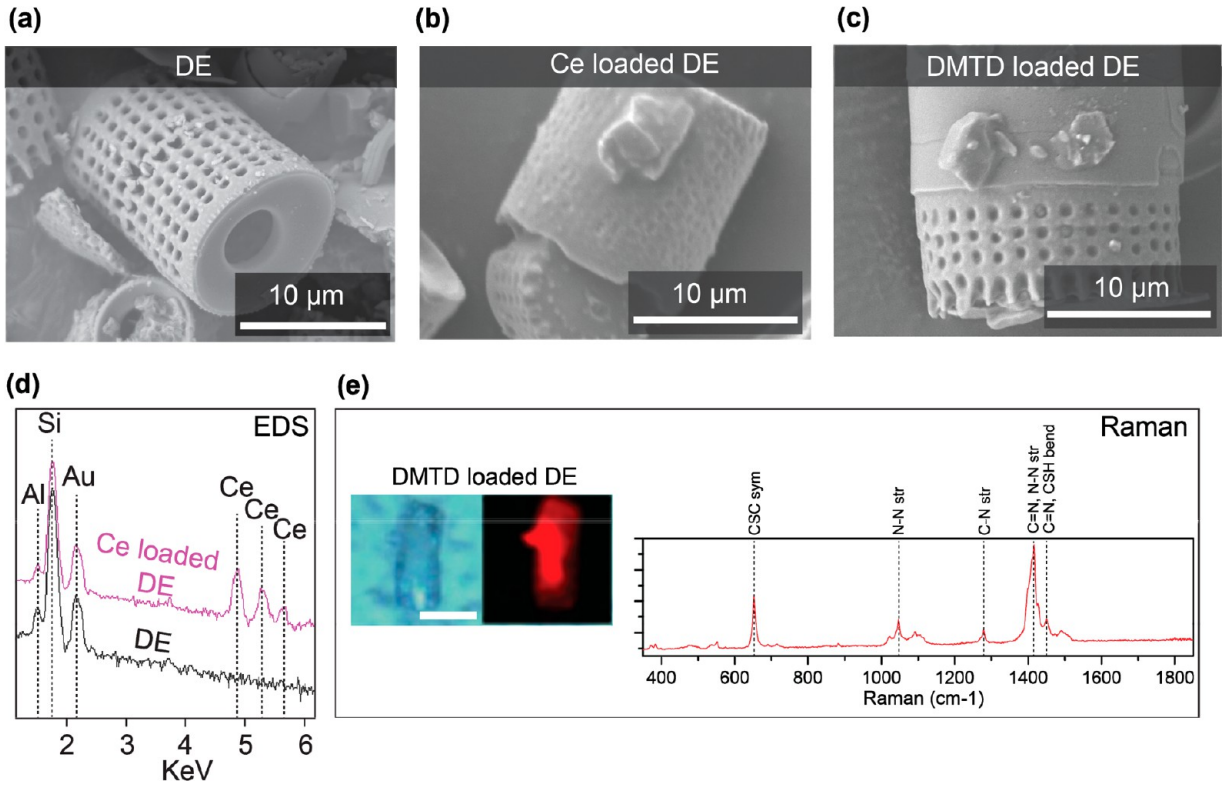

Figure 2. SEM images of DE microparticles before (a) and after inhibitor loading with $Ce(NO_3)_3$ (b) and DMTD (c). EDS spectra of the Ce-loaded DE (d) and Raman results of the DMTD-loaded DE (e).

https://dx.doi.org/10.1021/acsami.0c03368
ACS Appl. Mater. Interfaces 2020, 12, 23417−23431

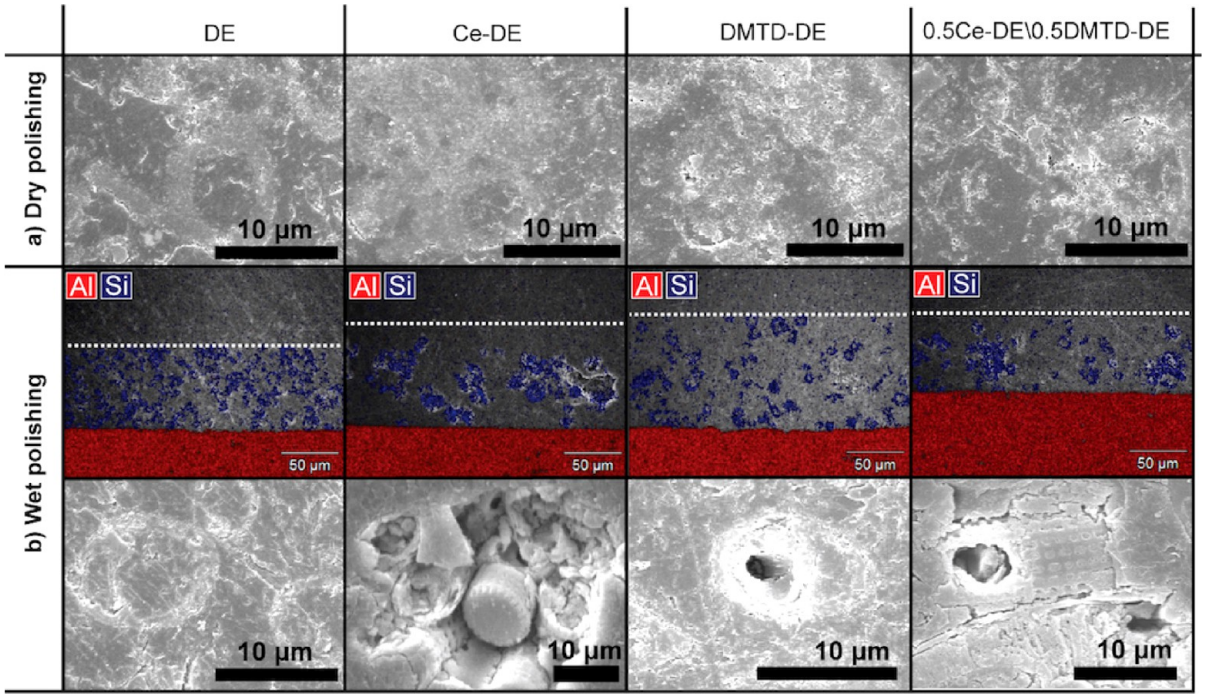

Figure 3. SEM and SEM/EDS micrographs of the coating cross sections after dry (a) and wet (b) polishing. The white dotted line highlights the interface between the coating and the casting resin. Blue regions indicate the presence of DE particles, and the red regions indicate the AA2024-T3 substrate.

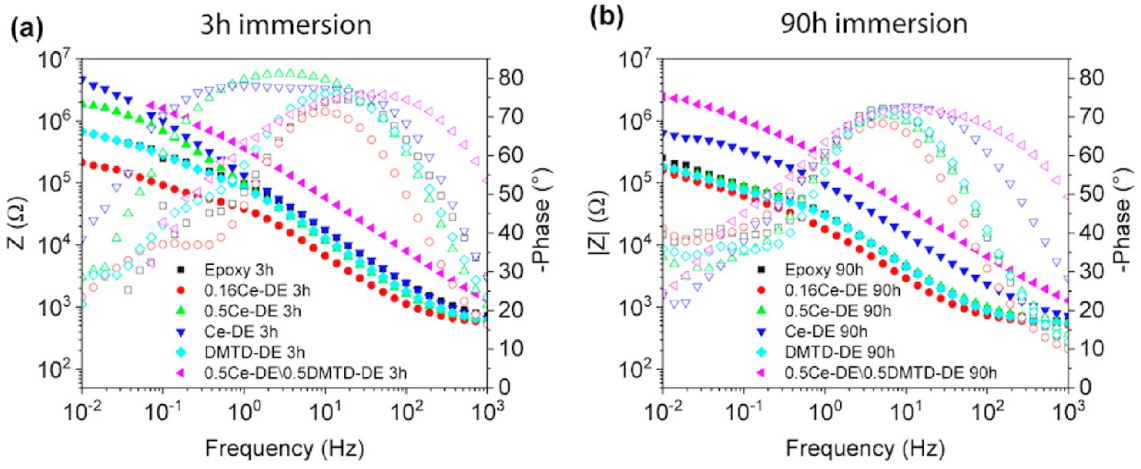

Figure 4. Bode plots (total impedance and phase angle as a function of frequency) of six scribed coatings after immersion in 200 mL/cm^2 0.05 M NaCl for 3 h (a) and 90 h (b). Unstable points at low frequencies have been removed in accordance with large Kramers−Kronig residual errors.

lowest cerium content (0.16Ce-DE) shows lower total impedance than does the epoxy nonloaded coating, which in turn is similar to the total impedance of the sample containing only DMTD (DMTD-DE). This indicates a low degree of corrosion protection in these three samples. Despite the impedance loss over time in all cases (see Figure S2, time evolution of impedance at 0.01 Hz), the overall trend shown in Figure 4b does not change during the 90 h immersion. As seen in Figure 4b, the 0.5Ce-DE\0.5DMTD-DE and Ce-DE coatings show significantly higher impedance values over the whole frequency range and the absence of pitting evidence at low frequencies based on the phase angle. These results confirm good corrosion protection under immersion conditions and are in agreement with our previously reported work with Ce-loaded DE.[22] While high impedance values at low and medium frequencies are often used to describe the degree of corrosion protection,[16,36,37] this assumption is not always valid for the inhibitors used in this work.[27] Highly resolved optical measurements during immersion help to improve the interpretation of such signals.

Figure 5 shows optical micrographs and color-gradient maps resulting from the image analysis at selected immersion times as obtained with the real-time optical-electrochemical setup. The color-gradient images allow one to visualize the severity of the local surface changes over time (i.e., effect of pitting, dealloying, inhibition, and oxide formation), in which darker colors relate to higher surface changes (i.e., higher degradation or oxide buildup). The original images can be found in Figure S3.

https://dx.doi.org/10.1021/acsami.0c03368
ACS Appl. Mater. Interfaces 2020, 12, 23417−23431

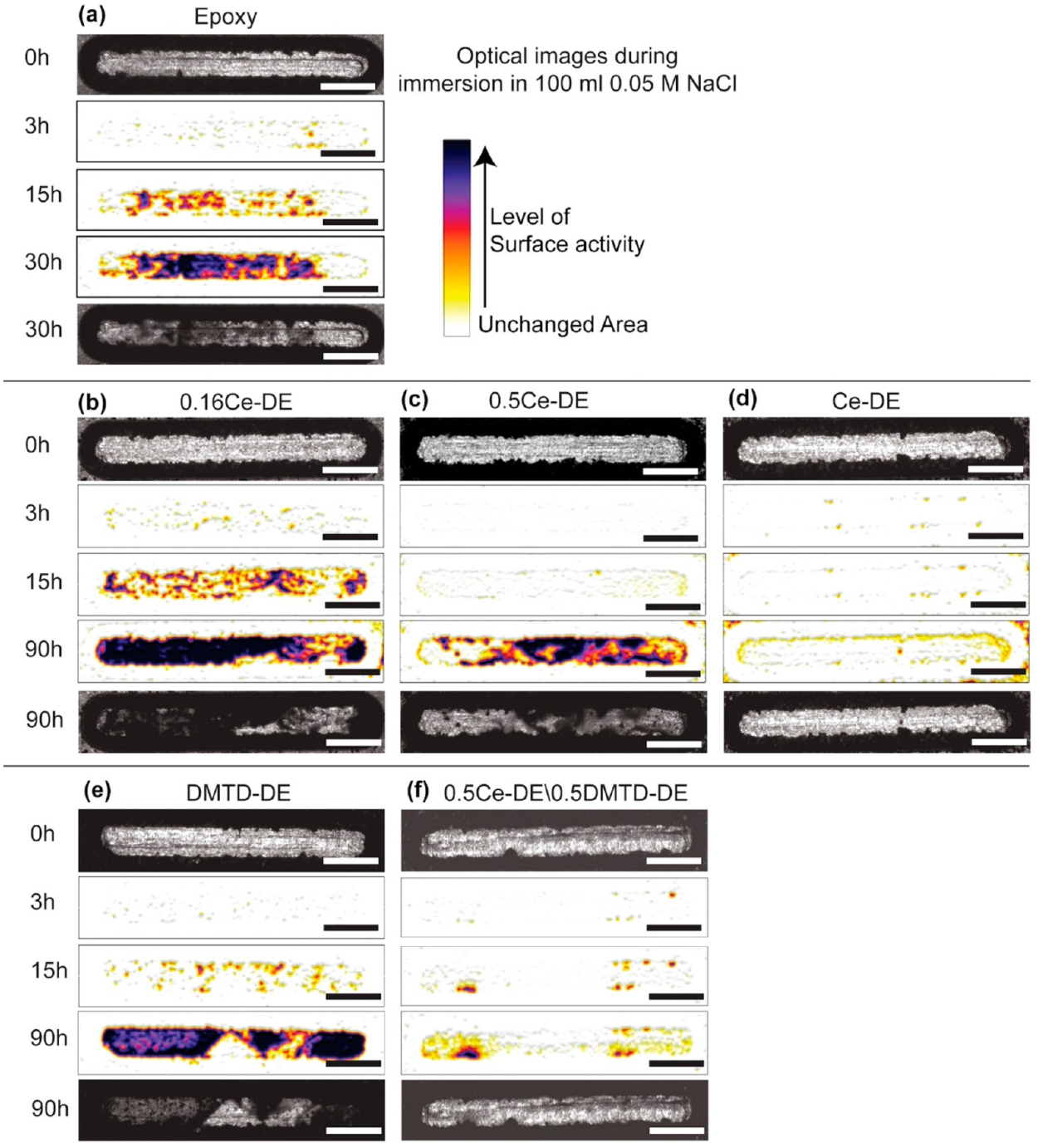

Figure 5. Optical images of six coated systems obtained with the real-time optical-electrochemical setup at 0, 3, 15, and 90 h immersion. Color images are the result of the implementation of the optical image analysis protocol. Scale bars represent 1 mm.

At 3 h of immersion, the noninhibited epoxy coating (Figure 5a) already shows the presence of multiple gray and yellow spots with diameters between 5 and 50 μm together with a couple of larger red-colored spots with diameters above 50 μm. The smaller gray-yellow locations can be related to initiation of local corrosion processes (e.g., intermetallic dissolution and trenching),[38] while larger red areas relate to pitting and early stage cooperative corrosion.[39,40] After 15 h of immersion, large dark-purple and black spots surrounded by red and yellow rings become evident, indicative of oxide deposits. As the dimension of this features is larger than the reported mean intermetallic particle diameter (2−5 μm), their appearance can be related to the start of subsurface corrosion processes (i.e., intergranular corrosion).[41,42] The dominance of black and purple areas all over the exposed scribe at 30 h immersion is indicative of generalized subsurface corrosion and cooperative corrosion (i.e., advanced corrosion). In agreement with this, the large amount of corrosion products at the scribe location did not allow further optical analysis at longer immersion times for this sample. Comparable results were obtained for the coating with the lowest cerium concentration of 0.16Ce-DE (Figure 5b), well in agreement with the EIS results.

The samples with the higher cerium content (0.5Ce-DE (Figure 5c) and Ce-DE (Figure 5d)) showed a clear delay in

https://dx.doi.org/10.1021/acsami.0c03368
ACS Appl. Mater. Interfaces 2020, 12, 23417−23431

the appearance of the first surface phenomenon related to corrosion (15 and 90 h, respectively). At 90 h of immersion, only the sample with the highest cerium content showed significant protection of the exposed metal surface based on the absence of detectable surface degradation in agreement with the EIS results.

Similarly to the Ce-containing samples, the DMTD-containing coatings (DMTD-DE (Figure 5e) and 0.5Ce-DE \0.5DMTD-DE (Figure 5f)) show a clear delay in the appearance of surface degradation. The apparent inhibiting effect observed in the DMTD-DE sample at times below 15 h could not be easily extracted from the EIS results (Figure 4), which highlights the importance of the real-time optical inspection. The absence of protection at immersion times longer than 15 h suggests that DMTD is too unstable at the surface or that there was insufficient DMTD release. However, the combination of cerium and DMTD (0.5Ce-DE \0.5DMTD-DE) shows significantly better results than the same amount of cerium alone (0.5Ce-DE) or higher contents of DMTD alone (DMTD-DE). Nevertheless, at 90 h immersion, signs of local degradation can be seen. Interestingly, the EIS results ranked this sample as the best despite the appearance of surface attack, while the Ce-DE sample showed less optically detectable surface attack and lower impedance, once more highlighting the need for in situ optics while electrochemical tests are being performed for a better understanding of the ongoing degradation/protection processes.

Besides a qualitative analysis, the optical data can be used to obtain quantitative degradation kinetics. Figure 6 shows the percentage of changed area in time for the studied coatings.

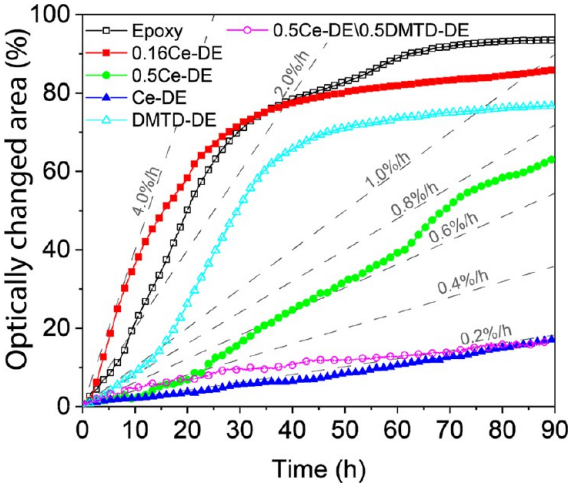

Figure 6. Time evolution of the optically detectable surface changes after image data treatment of the six coating systems. The gray dashed lines are added to give an impression of different degradation rates (%/h) so the reader can easily identify degradation rates for each coating during a specific exposure time.

As seen in Figure 6, the noninhibited system and the coating with low cerium content (0.16Ce-DE) show fast degradation kinetics (2−4% h^{-1}), comparable to those previously reported for noninhibited AA2024-T3 exposed to similar salt concentrations.[22,27] Despite the initial differences in degradation kinetics, both systems reached about 70% changed area within 30 h immersion. The faster degradation for the 0.16Ce-DE sample suggests that very low inhibitor concentrations may promote corrosion processes such as pitting. Similar results were previously described for coatings containing chromates below a critical amount.[43]

The coatings with higher cerium content (0.5Ce-DE and Ce-DE) showed 1 order of magnitude slower degradation kinetics (0.2−0.4% h^{-1}) during the first 20 h of immersion. Between 20 and 60 h of immersion, the changed-area growth kinetics for the 0.5Ce-DE tripled (0.6−0.8% h^{-1}), which suggests a drop in the inhibiting power of this coating. The sample with the highest cerium content (Ce-DE) maintained constant and low changed-area growth kinetics during the whole immersion time (0.2% h^{-1}).

The DMTD coatings (DMTD-DE and 0.5Ce-DE \0.5DMTD-DE) also have significantly slower changed-area growth kinetics (0.4−1.0% h^{-1}) during the first 15 h as compared to the epoxy system, confirming that the local corrosion processes are inhibited during this period. After 15 h, the kinetics increase for DMTD-DE, reaching values similar to those of the unprotected coatings (2.5% h^{-1}). These results once more indicate that DMTD was released and inhibited the corrosion process during the first hours of immersion, but that this effect was lost after 15 h most likely due to insufficient release of DMTD and/or lack of stability at the metal surface. However, the coating with two inhibitors (0.5Ce-DE \0.5DMTD-DE) showed an interesting decrease in the degradation growth kinetics after 15 h (from 0.4 to 0.2% h^{-1}), thereby reaching values similar to those of the coating with twice the cerium content (Ce-DE). This highlights the synergy between the Ce and DMTD and is in good agreement with previous studies reporting on this effect.[16,44] It is nevertheless important to note that the actual mechanism for this synergy is not yet fully understood.

3.3. Spatial and Temporally Resolved Local Corrosion Processes: Exposure to Small Electrolyte Volumes per Exposed Damaged Area. Figure 7 shows the oxygen concentration evolution during the first 15 h of immersion. A measurement on a coating without inhibitors (DE) is used as

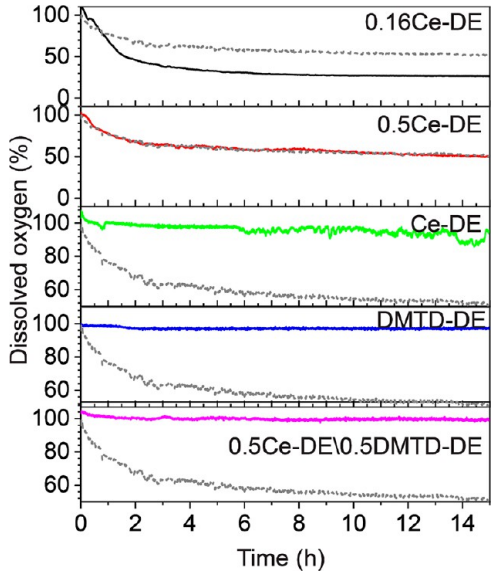

Figure 7. Time-evolution of dissolved oxygen concentration at 50 μm above the scribe during exposure to 20 mL of 0.05 M NaCl. A measurement on a coating without inhibitors (DE) is used as the negative control and is shown as a gray dotted line.

https://dx.doi.org/10.1021/acsami.0c03368
ACS Appl. Mater. Interfaces 2020, 12, 23417−23431

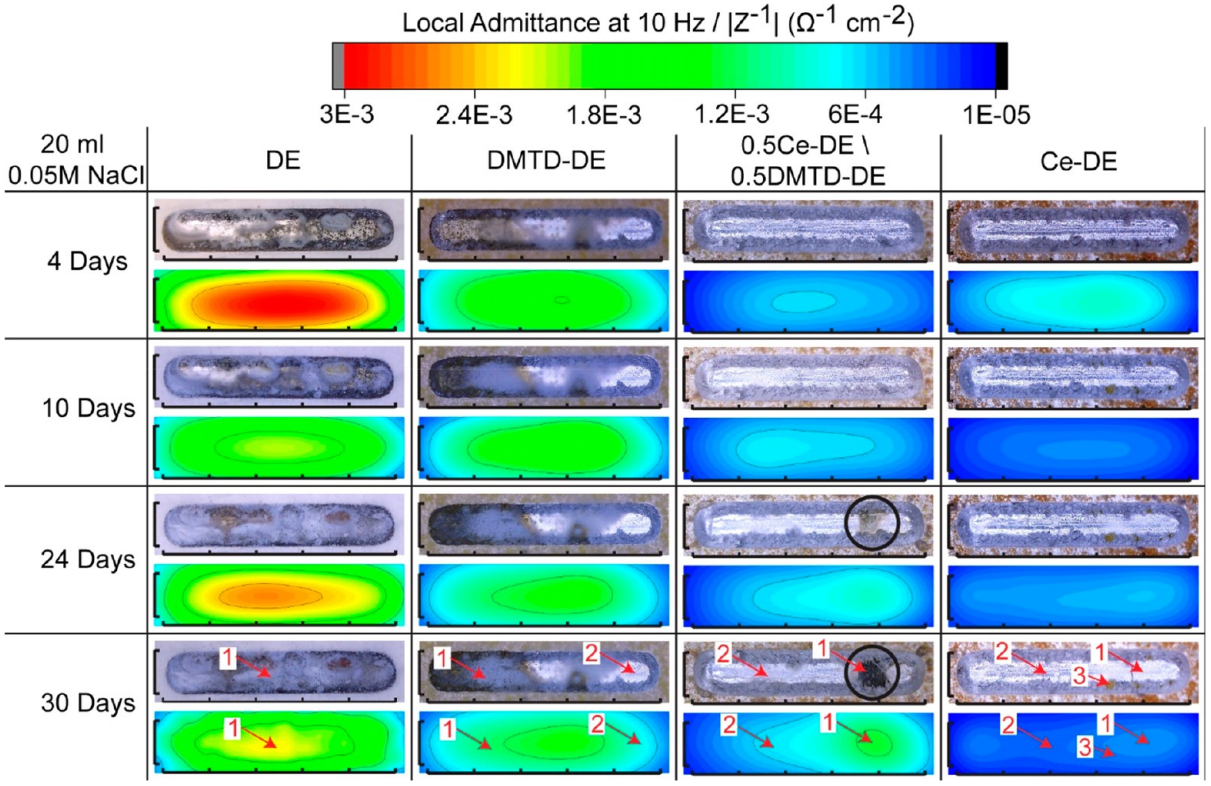

Figure 8. Representative LEIM results (admittance modulus $|Z^{-1}|$ maps) obtained at 10 Hz and 100 μm above the scribed coating and the corresponding in situ optical images as a function of the immersion time. LEIM map resolution is 0.075 × 0.100 mm with 0.1 mm step size (960 points per map). The probe-to-sample distance was identical in all cases (100 ± 1 μm above the coating). Arrows and numbers indicate the locations where postexposure SEM/EDS analysis was performed. Distance between ticks in the *x*-axis of the images correspond to 1 mm.

negative control and is shown as a gray dotted line in Figure 7. Although the tests were performed at the center of the damage and they might therefore not be representative of the whole scratch, there was very good agreement with the EIS results as discussed further on. These results reveal certain key differences as a function of the inhibitor type and concentration used. Higher cerium contents (Ce-DE) lead to lower oxygen concentration depletion but also more unstable signals after the first 6 h of immersion. When the organic inhibitor DMTD was used, with or without cerium (i.e., DMTD-DE and 0.5Ce-DE\0.5DMTD-DE), very stable high oxygen concentrations were measured.

Low cerium concentrations (0.16Ce-DE) show a significant drop in O_2 concentration with the immersion time, even sharper than the DE coating without inhibitors (gray dotted line). Such an O_2 drop appeared faster (within the first 5 h) and more pronounced (reaching 25%) for the lowest cerium content when compared to the drop observed at higher Ce contents or in the presence of DMTD, thereby confirming that the sharp drop in oxygen consumption is related to the presence of redox processes related to corrosion. As shown in previous works,[29,45] this oxygen drop can be related to the oxygen consumption in the cathodic reactions involved in the corrosion process, which, depending on the pH and thermodynamic local conditions, will mainly appear as reactions 3 and 4:

$$O_2 + 2H_2O + 4e^- \rightarrow 4OH^- \quad (3)$$

$$O_2 + 4H^+ + 4e^- \rightarrow 2H_2O \quad (4)$$

The level at which the oxygen concentration reaches an equilibrium can be directly related to the balance between the oxygen consumption due the redox reactions at the metal surface and the diffusion-driven oxygen replenishment from the electrolyte and surrounding air. Considering this, the oxygen measurement for 0.16Ce-DE is in perfect agreement with the results shown in Figures 5 and 6 where the lowest cerium content led to faster degradation kinetics in the first hours of immersion as compared to the coating without any inhibitor present (even when different samples were used). This suggests that cerium contents below a so far unspecified minimum can lead to increased corrosion rates. However, the coating with 3 times more cerium content (0.5Ce-DE) shows almost the same oxygen consumption as compared to the coating without any inhibitors, while the results shown in Figures 5 and 6 for this coating did show signs of inhibition. This indicates that the oxygen depletion rate due to the oxidation process has been reduced due to the presence of cerium and is similar to the oxygen replenishment rate, thereby indicating some inhibiting effect in good agreement with the EIS tests.

The coating with the highest level of cerium (Ce-DE) showed a sharp oxygen depletion peak during the first hour of immersion followed by full replenishment, which remained stable until 6 h of immersion. This first drop of oxygen and replenishment seems to be in good agreement with the protection mechanism of cerium ions, which have been reported to be efficient inhibitors after an initiation period of 30−180 min immersion.[46−48] After 6 h, reproducible oxygen fluctuations around the 80−100% oxygen concentration appeared. These fluctuations are here attributed to processes

https://dx.doi.org/10.1021/acsami.0c03368
ACS Appl. Mater. Interfaces 2020, 12, 23417−23431

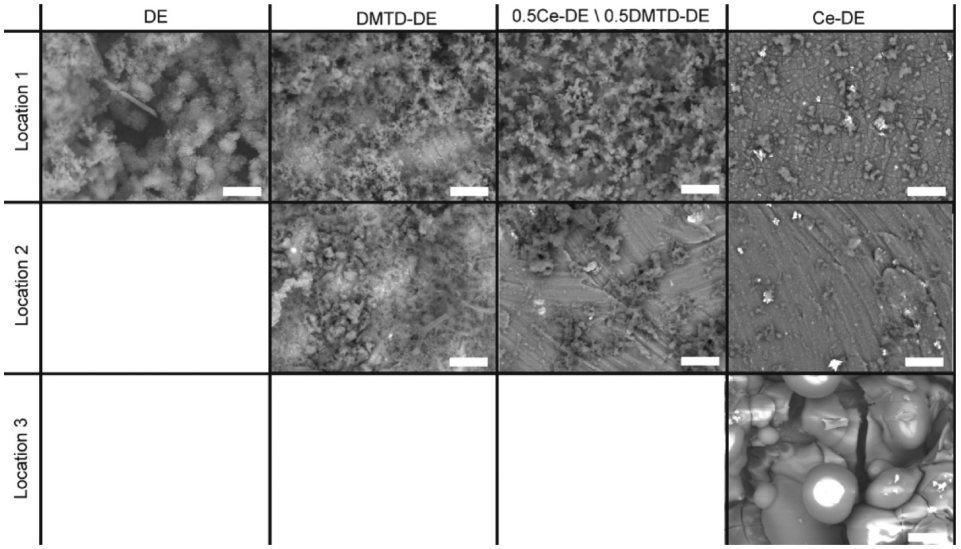

Figure 9. SEM micrographs in BSE mode after 30 days of immersion at the locations marked with arrows and numbers in Figure 8. Scale bar represents 10 μm.

Table 3. EDS Analysis of the Marked Locations in Figure 8 and Shown in Figure 9[a]

sample − location	O	Al	Cu	Zn	Mg	Cl	S	Ce
DE − 1	70.9	26.2		2.5				
DMTD-DE − 1	73.9	24.1					1.3	
DMTD-DE − 2	35.3	61.9	1.4		1.1			
0.5Ce-DE/0.5DMTD-DE − 1	70.4	24.4				1.2		3.4
0.5Ce-DE/0.5DMTD-DE − 2	56.7	38.13	1.5					3.5
Ce-DE − 1	61.4	25.0	13.7					
Ce-DE − 2	75.3	25.0						
Ce-DE − 3	56.0	39.1			1.3			

[a]Results are shown in atom %. [b]Table shows the elements that were detected above 1 atom %.

related to corrosion initiation and inhibition such as (i) sudden redox events related to local activation of intermetallic particles followed by immediate passivation, or/and (ii) the deposition of cerium ions at cathodic sites and passive film growth through reaction 5[47] followed by fast oxygen replenishment via diffusion:

$$4Ce^{3+} + O_2 + 4OH^- + 2H_2O \rightarrow 4Ce(OH)_2^{2+} \quad (5)$$

The addition of DMTD highly hindered the oxygen depletion and led to very stable oxygen concentration profiles at the center for the scribe, thereby suggesting a strong effect of DMTD in hindering the redox reactions during the first 15 h of immersion in small electrolyte volumes, thus considering oxygen replenishment kinetics from solution and air.

Because the samples with low cerium content showed significant corrosion already during the first 4 days of immersion in all previous experiments, it was decided to monitor the local electrochemical signal distribution only for the best performing samples and one reference. The setup shown in Figure 1c allowed one to measure global EIS as well as local EIS. Both methods led to comparable results, see the Bode and Nyquist plots in Figure S4, which validate the impedance measurements near the metal surface as opposite to those of other local techniques such as SVET.[49] It was decided to perform the local impedance mapping (LEIM) at 10 Hz frequency in good agreement with the literature where this frequency is used to validate comparably damaged coating with LEIM.[30] At this frequency, the impedance values reflect the kinetics of charge transfer at the metal/electrolyte interface. Therefore, the measured impedance values should be proportional to the corrosion current through the Stern−Geary relation and thereby be a direct relation to the inhibition power of the different systems.[50] Moreover, this frequency is representative for the detection of different behaviors between samples, as can be seen in the Nyquist plots (Figure S4). Figure 8 shows a selection of the obtained LEIM results after 4, 10, 24, and 30 days and their related optical micrographs. All of the obtained original LEIM maps (including measurements performed at different days of immersion) can be found in Figures S5−S8.

When the LEIM tests were finished (30 days of immersion), an SEM-EDS analysis of the scribes was performed. The main locations of interest are marked with arrows and numbers in Figure 8. Figure 9 and Table 3 show backscattered SEM images and the composition by EDS in atom %, respectively, of these locations.

As can be seen in Figure 8, after 4 days of immersion, clear oxides are visible in the DE and DMTD-DE samples accompanied by high admittance values (red and green colors). These results under small electrolyte volumes are similar to the previous optical and electrochemical results in large electrolytes (Figures 4−6) that show high surface activity and low impedance values well before 4 days of immersion. As can be seen in the optical images, the amount of oxide products in the noninhibited DE sample kept increasing with the immersion time to grow as a thick heterogeneous layer

https://dx.doi.org/10.1021/acsami.0c03368
ACS Appl. Mater. Interfaces 2020, 12, 23417−23431

containing Al_2O_3 and traces of ZnO (Figure 9 and Table 3), which is in good agreement with previous long-term exposure measurements to 0.05 M NaCl for AA2024-T3.[48] At 10 days of immersion, the thick aluminum oxide layer already masked the metal surface to the local probe, which resulted in a slight decrease of the local admittance.

Interestingly, the DMTD sample did not show this massive oxide growth. These findings combined with no oxygen concentration drop during the first hours (Figure 7) suggest that DMTD-loaded DE is able to partially protect the metal surface during the first hours of immersion. At longer times, nevertheless (beyond 1 day of immersion), the protection is deactivated and corrosion is initiated. However, the formed oxides remained stable at least between 10 and 30 days of immersion, limiting further degradation in a not yet fully understood process. The SEM-EDS analysis of the samples after 30 days of immersion (Figure 9) confirmed the presence of thin granular structures primarily containing Al and O (locations 1 and 2) with traces of sulfur from the DMTD (location 1), copper (location 2), and magnesium (location 2). Even when considering the quantification limitations of EDS, at location 2, an area that remained bright during the 30 days of immersion, the amount of detected oxygen resulted as below the stoichiometric values for pure aluminum oxides or hydroxides, thereby suggesting lower levels of oxidation (i.e., a thinner layer) and a positive effect of the corrosion inhibitor.

The coating containing both cerium- and DMTD-loaded DE (0.5Ce-DE\0.5DMTD-DE) shows a significantly lower amount of surface changes (optical images) together with low admittance values (blue colors) in time. This is a clear sign of high levels of active corrosion protection at large scribes. Despite the obvious good performance, at 24 days of immersion, a region showing optically detectable changes was observed (marked with a black circle in Figure 8). This area slowly but steadily became darker and bigger with the immersion time. At the end of the immersion period, the SEM-EDS analysis of this area (location 1) confirmed the presence of oxide features comparable to those observed in the DMTD-DE sample, although with a significant amount of detectable cerium (>3 at. %). A different location apparently not attacked by corrosion (location 2 for this sample in Figure 8) showed a significantly lower amount of oxygen, comparable cerium content, and traces of copper (Table 3). Considering the metal−oxygen atomic ratios of Ce_2O_3, $Ce(OH)_3$, Al_2O_3, and $Al(OH)_3$, these results suggest the presence of a cerium oxide layer at these locations. The absence of sulfur traces could be due to the inhibitor being below the detection limit of SEM-EDS. Considering the limited corrosion protection levels achieved with the samples 0.5Ce-DE (Figures 6 and 7) and DMTD-DE (Figure 8), the results are a clear indication of a significant synergetic effect between DMTD and cerium, at least when present in DE containers.

A more remarkable result was obtained for the Ce-DE sample. This coating remained stable with no obvious sign of degradation at the scribe during the whole duration of the experiment (30 days). Only small changes in admittance (off-centered local maxima) were measured at long immersion times as indicated by arrows in Figure 8. The SEM-EDS analysis at this location (location 1 in Figure 8 for this sample) showed a homogeneous but cracked thin layer similar to those of cerium conversion layers[51] and for excessive growth of Ce-containing precipitates.[52] Nevertheless, no clear signs of cerium were detected by SEM-EDS or Raman spectroscopy. The compositional analysis at this location showed a composition close to $Al(OH)_3$ with copper levels higher than expected for AA2024-T3 (i.e., max 5 wt %), thereby suggesting the deposition from dealloyed copper-rich intermetallic particles. The EDS analysis at two other locations (locations 2 and 3) also did not confirm the presence of cerium despite the clear smooth surface at location 2. Location 3, however, showed significant amounts of Mg, which together with the low amount of oxygen could indicate the formation of a Mg−Al oxide. It should be noted that the low corrosion activity at the scribe was accompanied by the absence of delamination during the whole immersion period as indicated by the stability of the admittance local maxima (Figure S9) and the different optical images. To the best of our knowledge, and despite the lack of evidence of the presence of cerium at the scribe, these remarkably high levels of protection of large scribes (1 mm wide and 0.35 mm deep) for such long immersion times (≥30 days) have only been reported for Cr(VI)-containing coatings such as commercial coatings containing significantly higher amounts of inhibitor (e.g., 16 wt % $SrCrO_4$[30]).

3.4. Effect of Electrolyte Volume per Exposed Area on the Corrosion Protection. The optical-electrochemical analysis using large volume-to-exposed area ratios (200 mL/cm^2) as exposed in Figure 6 shows that a higher content of cerium-loaded particles or the partial replacement of cerium by DMTD led to higher levels of corrosion inhibition. It should be noted that the remarkable protection at large damages in the case of the best performing coatings, Ce-DE and 0.5Ce-DE\0.5DMTD-DE, is achieved at very low active inhibitor contents (Table 1). Nevertheless, the continuous increase of optically detectable surface changes measured during the first 4 days of immersion suggests that the protective effect will eventually be (partially) lost as it is not enough to fully stop the degradation growth (corrosion) in the presence of large electrolyte volumes. Interestingly, the oxygen measurements and LEIM tests performed under smaller ratios of electrolyte (6.67 mL/cm^2) showed efficient protection at longer immersion times. Under small electrolyte ratios, DMTD-DE showed a good degree of protection during the first 15 h of immersion, while Ce-De and 0.5Ce-DE\0.5DMTD-DE maintained their high levels of protection well beyond 4 days of immersion. Despite the good results when exposed to low volumes, the two best performing samples also start showing some signs of protection loss at around 30 days of immersion. The eventual loss of protection with the immersion time suggests an insufficient inhibitor supply at the damaged site to cope with the apparent stability loss of the inhibiting layer on the metal surface, these effects being more identifiable when large electrolytes are used. The results show that further studies are required to better understand the effect of electrolyte volume and inhibiting layer stability on the long-term protection while highlighting the need of continuous inhibitor supply.

3.5. Performance during Wet/Dry Cyclic Test. In the above sections, the potential of inhibitor-loaded exoskeletons to protect coated metals at large scribed sites for long immersion times was demonstrated with remarkable results. Nevertheless, most applications are expected to work under wet−dry cyclic exposure, which may affect the inhibiting behavior of anticorrosive coatings. In this last section, we performed a preliminary study of the effect of wet/dry cycles during the immersion period and compared the behavior to the

https://dx.doi.org/10.1021/acsami.0c03368
ACS Appl. Mater. Interfaces 2020, 12, 23417−23431

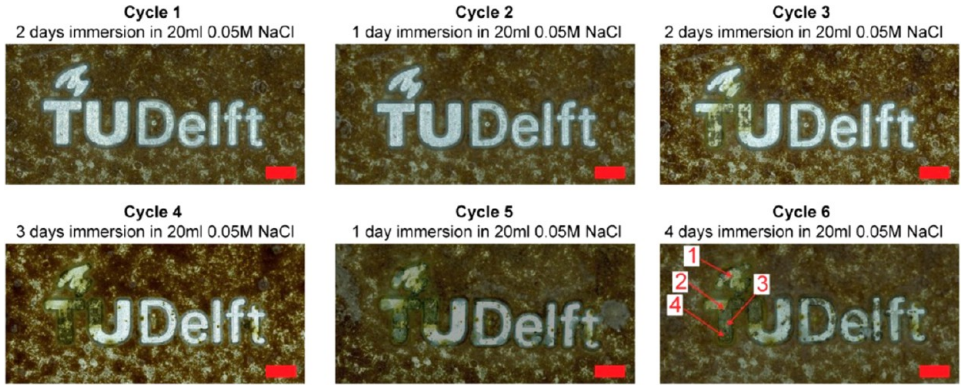

Figure 10. Optical images of the best performing coating according to continuous immersion (Ce-DE) with the "TU Delft" logo engraved. Micrographs show the evolution with the wet/dry cycles. For each immersion period, a fresh 20 mL of 0.05 M NaCl electrolyte solution was used. Locations marked with arrows and numbers were analyzed by SEM-EDS. Scale bars represent 1 mm.

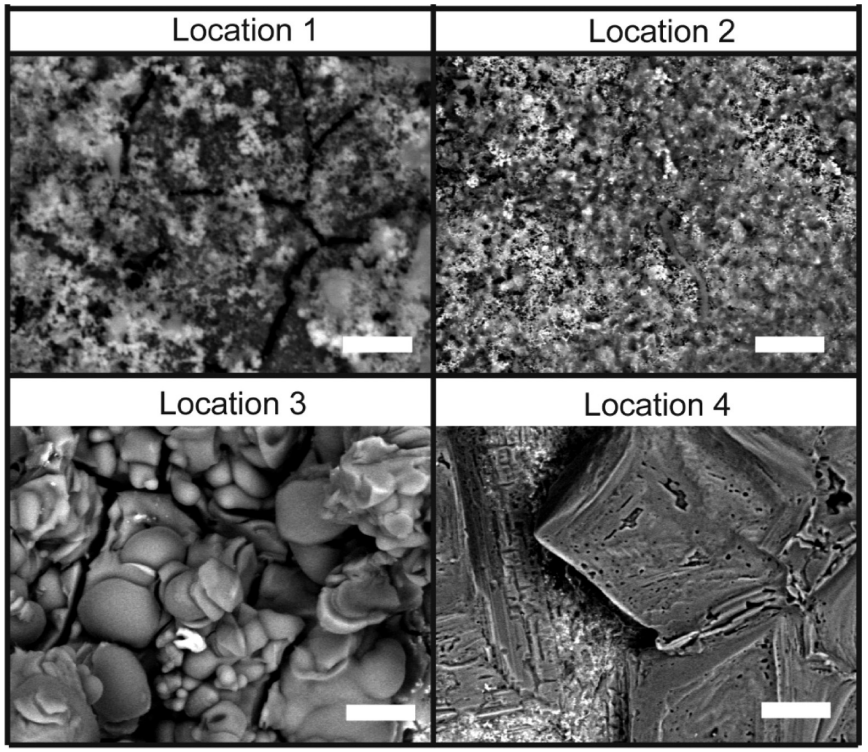

Figure 11. SEM micrographs in BSE mode for the Ce-DE coating after 6 wet/dry cycles. Locations correspond to those marked in Figure 10. Scale bar represents 10 μm.

continuous immersion results obtained for the best performing system (Ce-DE).

Figure 10 shows the optical images taken right after the drying step following the protocol exposed in the Experimental Section.

In Figure 10 it can be seen that the Ce-DE coating was able to protect the exposed aluminum surface (i.e., TUDelft logo) completely during the first two wet−dry cycles. After the second drying step followed by 3 days of immersion (third cycle), the first optical changes in the logo can be seen, roughly 25% of the exposed surface and mainly located at the widest scribed sites (letters T and U). Subsequent wet/dry cycles led to more surface changes until the test was stopped. After the cyclic test, roughly 50% of the metal surface (TUDelft logo) remained as bright as the nonexposed substrate. Interestingly, with the immersion time, the exposed metal area became yellowish, a clear indication of cerium oxide being formed on the surface.[53,54]

To identify the nature of the deposits visible in Figure 10, a number of SEM-EDS analyses were performed at the locations marked with arrows and numbers in Figure 10. The SEM micrographs and the EDS results can be seen in Figure 11 and Table 4, respectively.

As seen in Figure 11, features comparable to those observed in the Ce-DE sample exposed to continuous immersion during 30 days (Figure 9) are observed for locations 1−3 during wet/dry cycles. Nevertheless, the cyclic wet/dry test also led to the formation of a thicker and more pronounced, presumably protective, layer with significant traces of cerium at different locations (Table 4). Locations 1 and 3 can be considered comparable in terms of composition, although considerably higher levels of Cl, not measured during the continuous

https://dx.doi.org/10.1021/acsami.0c03368
ACS Appl. Mater. Interfaces 2020, 12, 23417−23431

Table 4. EDS Analysis for the Locations Shown in the SEM-BSE Images in Figure 11[a]

location	O	Al	Cu	Cl	Ce
1	42.7	17.3	2.9	4.8	4.1
2	60.3	29.1		6.6	
3	47.3	15.7		32.1	4.3
4	10.6			87.9	1.0

[a]Results are in atom %. [b]The table shows the elements that were detected above 1 atom %.

immersion tests, are detected at location 3. Despite these results, the most surprising structures are found in location 4. At this location, no Al was detected, while relatively big crystalline structures containing chlorine, cerium, and oxygen were observed. These crystalline structures remained after the exposed surface was washed with demi-water several times, thereby demonstrating their high stability. Notwithstanding the darkening and yellowing, the relatively low Al contents in all of the locations together with the high levels of oxygen and cerium suggest at least some partial stable passivation of the exposed metal surface by the cerium released from the Ce-DE particles. It is important to note that for these tests the precise procedure, such as additional rinsing steps between the wet–dry exposure, can have an effect on the degree of protection. Our results do however confirm a significantly different behavior when dry cycles are included in the exposure protocol and highlight the need for more dedicated studies including so-called wet/dry cycles.

4. CONCLUSIONS

Corrosion protection by inhibitor-loaded naturally occurring silica microparticles (i.e., diatomaceous earth) to protect wide and deep scribes (up to 1 mm wide and 350 μm deep) was studied. The diatomaceous earth particles were loaded with cerium nitrate and 2,5-dimercaptothiadiazole (DMTD). The corrosion inhibition performance of epoxy-amine coatings containing different amounts of loaded particles and corrosion inhibitors was then evaluated under continuous immersion and during cyclic (wet/dry) conditions using an in situ real-time optical electrochemical setup and local electrochemistry.

It was found that even when the loading of corrosion inhibitor in the diatomaceous earth is far from optimized (i.e., containing large free volumes), corrosion protection was achieved for at least 30 days of immersion in salt solution with coatings containing as low as 3.7 wt % active inhibiting component (i.e., Ce^{3+}). The coatings loaded only with an organic inhibitor (DMTD) did not result in significant corrosion protection possibly due to insufficient inhibitor release. Nevertheless, the use of a limited amount of DMTD together with cerium led to a remarkable increase in the efficiency, while coatings containing similar cerium content were unable to protect the damages for long times. This points at the synergy between the two inhibitors when loaded into diatomaceous earth. Nevertheless, the corrosion protection significantly reduces in terms of immersion time when the samples are exposed to larger electrolyte volumes. Finally, wet/dry cyclic tests showed that drying steps and cumulative supply of fresh electrolyte can increase the buildup of stable inhibitor-containing layers as compared to more commonly performed immersion testing. The long-term protection shows the potential of this technology as well as the need for tests other than continuous immersion to better understand the limitations and potential of upcoming novel anticorrosive concepts.

ASSOCIATED CONTENT

Supporting Information

The Supporting Information is available free of charge at https://pubs.acs.org/doi/10.1021/acsami.0c03368.

Active inhibitor component inside the coating, optical-electrochemical study, local electrochemical impedance spectra, LEIM results, gradient of admittance for scribed coatings, and an additional reference (PDF)

AUTHOR INFORMATION

Corresponding Authors

Paul J. Denissen − *Novel Aerospace Materials Group, Faculty of Aerospace Engineering, Delft University of Technology, Delft 2629 HS, The Netherlands;* orcid.org/0000-0003-1201-2765; Email: p.j.denissen@tudelft.nl

Santiago J. Garcia − *Novel Aerospace Materials Group, Faculty of Aerospace Engineering, Delft University of Technology, Delft 2629 HS, The Netherlands;* orcid.org/0000-0002-2211-9972; Email: s.j.garciaespallargas@tudelft.nl

Authors

Viacheslav Shkirskiy − *Chimie ParisTech, PSL Research University, CNRS, Institut de Recherche de Chimie Paris (IRCP), Paris F-75005, France*

Polina Volovitch − *Chimie ParisTech, PSL Research University, CNRS, Institut de Recherche de Chimie Paris (IRCP), Paris F-75005, France;* orcid.org/0000-0001-5729-9830

Complete contact information is available at: https://pubs.acs.org/10.1021/acsami.0c03368

Notes

The authors declare no competing financial interest.

ACKNOWLEDGMENTS

S.J.G. and P.J.D. thank the Faculty of Aerospace Engineering at the Delft University of Technology for financial support, Prof. Sybrand van der Zwaag for his continued support and constructive discussions, and Akzo Nobel for providing the epoxy/amine resins. We thank the European Federation for Corrosion (EFC) and the EUROCORR 2018 Young Scientific Grant for awarding a travel grant to P.J.D., thereby enabling a fruitful collaboration between our research groups.

REFERENCES

(1) Surface Engineering Association. Surface Engineering Association, REACH and the impact of Hexavalent Chromium. *Surf. Eng. Assoc.* **2019**.

(2) Eichinger, E.; Osborne, J.; Van Cleave, T. Hexavalent chromium elimination: An aerospace industry progress report. *Met. Finish.* **1997**, *95*, 36.

(3) Jakab, M. A.; Presuel-Moreno, F.; Scully, J. R. Critical concentrations associated with cobalt, cerium, and molybdenum inhibition of AA2024-T3 corrosion: Delivery from Al-Co-Ce(-Mo) alloys. *Corrosion* **2005**, *61*, 246–263.

(4) Shi, H.; Han, E. H.; Liu, F. Corrosion protection of aluminium alloy 2024-T3 in 0.05M NaCl by cerium cinnamate. *Corros. Sci.* **2011**, *53*, 2374–2384.

(5) Yasakau, K. A.; Zheludkevich, M. L.; Lamaka, S. V.; Ferreira, M. G. S. Mechanism of corrosion inhibition of AA2024 by rare-earth compounds. *J. Phys. Chem. B* **2006**, *110*, 5515–5528.

(6) Gui, J.; Devine, T. M. Influence of lithium on the corrosion of aluminum, Scr. *Scr. Metall.* **1987**, *21*, 853−857.
(7) Rangel, C. M.; Travassos, M. A. The passivation of aluminium in lithium carbonate/bicarbonate solutions. *Corros. Sci.* **1992**, *33*, 327−343.
(8) Dieleman, C. D.; Denissen, P. J.; Garcia, S. J. Long-Term Active Corrosion Protection of Damaged Coated-AA2024-T3 by Embedded Electrospun Inhibiting Nanonetworks. *Adv. Mater. Interfaces* **2018**, *5*, 1800176.
(9) Visser, P.; Meeusen, M.; Gonzalez-Garcia, Y.; Terryn, H.; Mol, J. M. C. Electrochemical evaluation of corrosion inhibiting layers formed in a defect from lithium-leaching organic coatings. *J. Electrochem. Soc.* **2017**, *164*, C396−C406.
(10) Laird, J. S.; Visser, P.; Ranade, S.; Hughes, A. E.; Terryn, H.; Mol, J. M. C. Li leaching from Lithium Carbonate-primer: An emerging perspective of transport pathway development. *Prog. Org. Coat.* **2019**, *134*, 103−118.
(11) Chen, W.; Luo, H. Q.; Li, N. B. Inhibition effects of 2,5-dimercapto-1,3,4-thiadiazole on the corrosion of mild steel in sulphuric acid solution. *Corros. Sci.* **2011**, *53*, 3356−3365.
(12) Abdolah Zadeh, M.; Tedim, J.; Zheludkevich, M.; van der Zwaag, S.; Garcia, S. J. Synergetic active corrosion protection of AA2024-T3 by 2D- anionic and 3D-cationic nanocontainers loaded with Ce and mercaptobenzothiazole. *Corros. Sci.* **2018**, *135*, 35−45.
(13) Chadwick, D.; Hashemi, T. Electron spectroscopy of corrosion inhibitors: Surface films formed by 2-mercaptobenzothiazole and 2-mercaptobenzimidazole on copper. *Surf. Sci.* **1979**, *89*, 649−659.
(14) Ferrer, E. L.; Rollon, A. P.; Mendoza, H. D.; Lafont, U.; Garcia, S. J. Double-doped zeolites for corrosion protection of aluminium alloys. *Microporous Mesoporous Mater.* **2014**, *188*, 8−15.
(15) Williams, G.; Coleman, A. J.; McMurray, H. N. Inhibition of Aluminium Alloy AA2024-T3 pitting corrosion by copper complexing compounds, Electrochim. *Electrochim. Acta* **2010**, *55*, 5947−5958.
(16) Snihirova, D.; Lamaka, S. V.; Taheri, P.; Mol, J. M. C.; Montemor, M. F. Comparison of the synergistic effects of inhibitor mixtures tailored for enhanced corrosion protection of bare and coated AA2024-T3. *Surf. Coat. Technol.* **2016**, *303*, 342−351.
(17) Twite, R. L.; Bierwagen, G. P. Review of alternatives to chromate for corrosion protection of aluminum aerospace alloys. *Prog. Org. Coat.* **1998**, *33*, 91−100.
(18) Shi, X.; Nguyen, T. A.; Suo, Z.; Liu, Y.; Avci, R. Effect of nanoparticles on the anticorrosion and mechanical properties of epoxy coating. *Surf. Coat. Technol.* **2009**, *204*, 237−245.
(19) Loison, P.; Debout, V.; Groult, H.; Creus, J.; Touzain, S. Incorporation of silica nanocontainers and its impact on a waterborne polyurethane coating. *Mater. Corros.* **2019**, *70*, 1884−1899.
(20) Sharmila, R.; Selvakumar, N.; Jeyasubramanian, K. Evaluation of corrosion inhibition in mild steel using cerium oxide nanoparticles. *Mater. Lett.* **2013**, *91*, 78−80.
(21) Borisova, D.; Möhwald, H.; Shchukin, D. G. Influence of embedded nanocontainers on the efficiency of active anticorrosive coatings for aluminum alloys part I: Influence of nanocontainer concentration. *ACS Appl. Mater. Interfaces* **2012**, *4*, 2931−2939.
(22) Denissen, P. J.; Garcia, S. J. Cerium-loaded algae exoskeletons for active corrosion protection of coated AA2024-T3. *Corros. Sci.* **2017**, *128*, 164−175.
(23) Homborg, A. M.; Van Westing, E. P. M.; Tinga, T.; Ferrari, G. M.; Zhang, X.; De Wit, J. H. W.; Mol, J. M. C. Application of transient analysis using Hilbert spectra of electrochemical noise to the identification of corrosion inhibition. *Electrochim. Acta* **2014**, *116*, 355−365.
(24) Ma, X.; Qian, B.; Zhang, J.; Xu, W.; Jiang, Q.; Zheng, M.; Ma, F.; Hou, B. The inhibition effect of polyaspartic acid and its mixed inhibitor on mild steel corrosion in seawater wet/dry cyclic conditions. *Int. J. Electrochem. Sci.* **2016**, 3024.
(25) Visser, P.; Terryn, H.; Mol, J. M. C. On the importance of irreversibility of corrosion inhibitors for active coating protection of AA2024-T3. *Corros. Sci.* **2018**, *140*, 272−285.
(26) Saini, V.; von Tapavicza, M.; Eloo, C.; Braesch, K.; Wack, H.; Nellesen, A.; Schmidt, A. M.; García, S. J. Superabsorbent polymer additives for repeated barrier restoration of damaged powder coatings under wet-dry cycles: A proof-of-concept. *Prog. Org. Coat.* **2018**, *122*, 129−137.
(27) Denissen, P. J.; Garcia, S. J. Reducing subjectivity in EIS interpretation of corrosion and corrosion inhibition processes by in-situ optical analysis. *Electrochim. Acta* **2019**, *293*, 514−524.
(28) Denissen, P. J.; Homborg, A. M.; Garcia, S. J. Interpreting electrochemical noise and monitoring local corrosion by means of highly resolved spatiotemporal real-time optics. *J. Electrochem. Soc.* **2019**, *166*, C3275−C3283.
(29) Taryba, M. G.; Montemor, M. F.; Lamaka, S. V. Quasi-simultaneous Mapping of Local Current Density, pH and Dissolved O2. *Electroanalysis* **2015**, *27*, 2725−2730.
(30) Nguyen, A. S.; Pébère, N. A local electrochemical impedance study of the self-healing properties of waterborne coatings on 2024 aluminium alloy. *Electrochim. Acta* **2016**, *222*, 1806−1817.
(31) Shkirskiy, V.; Krasnova, A.; Sanchez, T.; Amar, A.; Vivier, V.; Volovitch, P. Development of anodic and cathodic blisters at a model Zn/epoxy interface studied using local electrochemical impedance. *Electrochem. Commun.* **2020**, *111*, 106633.
(32) Aw, M. S.; Bariana, M.; Yu, Y.; Addai-Mensah, J.; Losic, D. Surface-functionalized diatom microcapsules for drug delivery of water-insoluble drugs. *J. Biomater. Appl.* **2013**, *28*, 163−174.
(33) Thévenaz, P.; Ruttimann, U. E.; Unser, M. A pyramid approach to subpixel registration based on intensity. *IEEE Trans. Image Process* **1998**, *7*, 27−41.
(34) Huang, V. M.; Wu, S. L.; Orazem, M. E.; Pébre, N.; Tribollet, B.; Vivier, V. Local electrochemical impedance spectroscopy: A review and some recent developments. *Electrochim. Acta* **2011**, *56*, 8048−8057.
(35) Maiti, N. *RSC Adv.* **2016**, *6*, 62529−62539.
(36) Schem, M. *Corros. Sci.* **2009**, *51*, 2304.
(37) Lamaka, S. V. *Electrochim. Acta* **2007**, *52*, 7231.
(38) Boag, A.; Hughes, A. E.; Glenn, A. M.; Muster, T. H.; McCulloch, D. Corrosion of AA2024-T3 Part I: Localised corrosion of isolated IM particles. *Corros. Sci.* **2011**, *53*, 17−26.
(39) Hughes, A.; Muster, T. H.; Boag, A.; Glenn, A. M.; Luo, C.; Zhou, X.; Thompson, G. E.; McCulloch, D. Co-operative corrosion phenomena. *Corros. Sci.* **2010**, *52*, 665−668.
(40) Hughes, A. E.; Boag, A.; Glenn, A. M.; McCulloch, D.; Muster, T. H.; Ryan, C.; Luo, C.; Zhou, X.; Thompson, G. E. Corrosion of AA2024-T3 Part II: Co-operative corrosion. *Corros. Sci.* **2011**, *53*, 27−39.
(41) Glenn, A. M.; Muster, T. H.; Luo, C.; Zhou, X.; Thompson, G. E.; Boag, A.; Hughes, A. E. Corrosion of AA2024-T3 Part III: Propagation. *Corros. Sci.* **2011**, *53*, 40−50.
(42) Hughes, A. E.; Birbilis, N.; Mol, J. M. C.; Garcia, S. J.; Zhou, X.; Thompson, G. E. High Strength Al-Alloys: Microstructure, Corrosion and Principles of Protection. *Recent Trends in Processing and Degradation of Aluminium Alloys*; IntechOpen: London, UK, 2011; pp 223−262.
(43) Khaled, K. F. Electrochemical Evaluation of Environmentally Friendly Cerium Salt as Corrosion Inhibitor for Steel in 3.5% NaCl. *Int. J. Electrochem. Sci.* **2013**, *8*, 3974−3987.
(44) Snihirova, D. *Corros. Sci.* **2016**, *112*, 408.
(45) Taryba, M. G.; Van den Bergh, K.; De Strycker, J.; Dolgikh, O.; Deconinck, J.; Lamaka, S. V. Novel use of a micro-optode in overcoming the negative influence of the amperometric micro-probe on localized corrosion measurements. *Corros. Sci.* **2015**, *95*, 1−5.
(46) Rosero-Navarro, N. C.; Curioni, M.; Bingham, R.; Durán, A.; Aparicio, M.; Cottis, R. A.; Thompson, G. E. Electrochemical techniques for practical evaluation of corrosion inhibitor effectiveness. Performance of cerium nitrate as corrosion inhibitor for AA2024T3 alloy. *Corros. Sci.* **2010**, *52*, 3356−3366.
(47) Udoh, I. I.; Shi, H.; Liu, F.; Han, E. H. Synergistic Effect of 3-Amino-1,2,4-triazole-5-thiol and Cerium Chloride on Corrosion Inhibition of AA2024-T3. *J. Electrochem. Soc.* **2019**, *166*, C185−C195.

https://dx.doi.org/10.1021/acsami.0c03368
ACS Appl. Mater. Interfaces 2020, 12, 23417−23431

(48) Garcia, S. J. *Corros. Sci.* **2013**, *69*, 346.
(49) Upadhyay, V. *Prog. Org. Coat.* **2016**, *99*, 365.
(50) Snihirova, D. *Electrochim. Acta* **2012**, *83*, 439.
(51) Buchheit, R. G. *Corrosion* **2002**, *58*, 3.
(52) Coelho, L.B. *Corros. Sci.* **2018**, *130*, 177.
(53) Arnott, D. R. *Appl. Surf. Sci.* **1985**, *22-23*, 236.
(54) Matter, E. A. *Corros. Sci.* **2012**, *62*, 22.

https://dx.doi.org/10.1021/acsami.0c03368
ACS Appl. Mater. Interfaces 2020, 12, 23417−23431